

Spin-Selective Thermoelectric Transport in a Triangular Spin Ladder

Ranjini Bhattacharya^{1,*} and Souvik Roy^{2,3,†}

¹*Department of Condensed Matter and Materials Physics,*

S. N. Bose National Centre for Basic Sciences, JD-Block, Sector III, Salt Lake, Kolkata 700098, India

²*School of Physical Sciences, National Institute of Science Education and Research, Jatni 752050, India*

³*Homi Bhabha National Institute, Training School Complex, Anushaktinagar, Mumbai 400094, India*

(Dated: December 17, 2025)

We theoretically investigate spin-resolved thermoelectric transport in a triangular ladder geometry hosting antiferromagnetic spin alignment, where lattice topology and magnetic ordering jointly enable highly efficient spin-selective energy conversion. The inherent geometric frustration of the ladder, together with intrinsic spin-filtering mechanisms, is shown to promote a pronounced separation between spin channels. Implementing spin-dependent onsite modulations, such as binary asymmetric potentials, induces pronounced spin splitting in the transmission spectrum, enabling controlled spin-selective transport and highlighting the role of lattice engineering in tailoring spin-dependent thermoelectric response. Additional control is achieved through modulation of the hopping amplitudes, which activates multiple transport pathways and allows fine tuning of spin-dependent conduction. A detailed evaluation of charge and spin thermoelectric coefficients reveals a strong enhancement of the thermoelectric performance, with the dimensionless figure of merit ZT reaching large values in optimized parameter regimes. Notably, the spin figure of merit systematically surpasses its charge counterpart, underscoring the decisive role of lattice geometry and antiferromagnetic order in amplifying spin thermoelectric efficiency. Our findings provide a versatile theoretical platform for designing low-dimensional spin-caloritronic devices with enhanced functionality.

I. INTRODUCTION

The steadily increasing global energy demand, together with mounting environmental concerns and the finite nature of fossil fuel resources, has intensified the search for alternative technologies capable of delivering high energy efficiency and sustainability. In this pursuit, thermoelectric (TE) systems have gained renewed interest due to their ability to convert thermal gradients directly into electrical power using solid-state mechanisms, without the need for mechanical motion or auxiliary working media. This intrinsic simplicity renders TE devices highly reliable, compact, and well suited for precise thermal regulation, positioning them as attractive candidates for waste-heat recovery and thermal management applications^{1–6}. While the fundamental concepts underlying thermoelectricity date back to the discovery of the Seebeck and Peltier effects^{7,8}, the performance of existing thermoelectric materials remains far from optimal. Consequently, achieving a substantial enhancement of the dimensionless thermoelectric figure of merit, ZT , continues to be a central challenge and a key objective in the ongoing development of efficient thermoelectric materials and device architectures.

Nanostructuring has provided transformative opportunities in thermoelectric research by overcoming many of the intrinsic limitations associated with bulk materials. Low-dimensional quantum systems, including quantum dots, carbon nanotubes, molecular junctions, and quantum wires^{9–12}, have shown substantial enhancements in the thermoelectric figure of merit (ZT), enabling applications ranging from thermal rectification¹³ to microscale refrigeration. Advances in single-molecule electronics and heterojunction engineering have further expanded the design space for thermoelectric devices, offering structurally versatile, electronically tunable, and environmentally sustainable platforms. These develop-

ments underscore the potential of low-dimensional systems¹⁴ as building blocks for scalable energy-harvesting technologies. Nevertheless, achieving consistently high thermoelectric efficiency while maintaining precise control over spin- and charge-dependent transport^{15–18} remains a central challenge. In this context, we introduce a triangular ladder model with tailored spin orientations at selected sites, combined with modulated onsite energies and hopping amplitudes, to achieve controlled spin-resolved transport. This framework provides a promising route toward designing highly efficient spin-selective thermoelectric devices with tunable transport characteristics.

Motivated by these challenges, we propose a theoretical framework for spin-resolved transport based on a triangular ladder geometry. In this construction, the upper arm exclusively accommodates spin-up electrons, whereas the lower arm carries only spin-down electrons, effectively mapping the spin degree of freedom onto a spatial index. Introducing asymmetry between the two arms results in a controlled separation of the spin-resolved transmission channels, enabling spin-selective transport^{19–21} within a unified tight-binding formalism.

From a thermoelectric standpoint, achieving high spin-dependent performance requires minimizing the overlap between spin-up and spin-down transmission spectra while introducing sharp energy-dependent features. Within the Landauer–Büttiker formalism, these conditions directly enhance the spin-resolved Seebeck coefficient^{22–32} via the energy derivatives of the transmission functions. We show that such criteria can be systematically engineered by adjusting the microscopic parameters of the triangular ladder. Specifically, we consider two symmetry-breaking strategies. In the first approach, a binary lattice is introduced in which the onsite energies of the two spin channels differ, producing spin-dependent shifts in the transmission spectra. In the

second approach, the onsite energies are kept identical, while asymmetry is introduced through unequal hopping amplitudes along the upper and lower arms. Both mechanisms generate pronounced spin splitting in the transmission channels, creating favorable conditions for an enhanced spin thermoelectric response. We find in both the cases the spin TE coefficients surpass the charge counterpart, which is indeed a very desirable outcome.

This parameter-tunable transport framework offers a minimal yet highly flexible platform for controlling spin-dependent thermoelectric properties^{33,34}. By allowing independent adjustment of spin-resolved transmission channels within a coherent quantum transport scheme, the model provides a practical pathway for optimizing spin Seebeck coefficients^{35–38} and achieving substantially enhanced values of the spin thermoelectric figure of merit.

The paper is structured as follows. In Sec. I, we outline the motivation and objectives of the study. Sec. II introduces the triangular ladder model and the nonequilibrium Green's function (NEGF) based transport formalism^{39,40}. Sec. III presents a detailed discussion of the results, and Sec. IV concludes with a summary of the main findings and their implications.

II. QUANTUM FRAMEWORK FOR THERMOELECTRIC TRANSPORT: MODEL, HAMILTONIAN AND THEORETICAL FRAMEWORK

A. Model and Hamiltonian Formulation of Quantum Transport in Triangular Spin Ladder

The source and drain electrodes are maintained at slightly different temperatures, $T + \Delta T/2$ and $T - \Delta T/2$, which generates a finite thermal bias ΔT across the junction. To ensure analytical clarity and experimental relevance, we restrict our analysis to the linear-response regime by assuming that ΔT is sufficiently small. The central anti-ferromagnetic (AFM) chain is composed of atomic sites hosting localized magnetic moments, whose general orientation may be described by the polar angle θ_i and the azimuthal angle ψ_i . In the present study, we consider a simplified yet physically meaningful configuration in which all local moments are rigidly aligned along the $+Z$ direction. This alignment stabilizes a uniform ferromagnetic phase with complete spin polarization and a net magnetization oriented along $+Z$. Such an idealized setting, free from spin fluctuations and external perturbations, provides a transparent platform for examining how an intrinsically spin-polarized background controls spin-dependent transport and the associated thermoelectric response.

$$H = H_L + H_S + H_D + H_{tn} \quad (1)$$

where, H_L , H_S , H_D , and H_{tn} denote the Hamiltonians corresponding to the central chain, the source electrode, the drain electrode, and the tunneling coupling between the electrodes and the SSH chain, respectively. Each term encapsulates a specific physical component of the

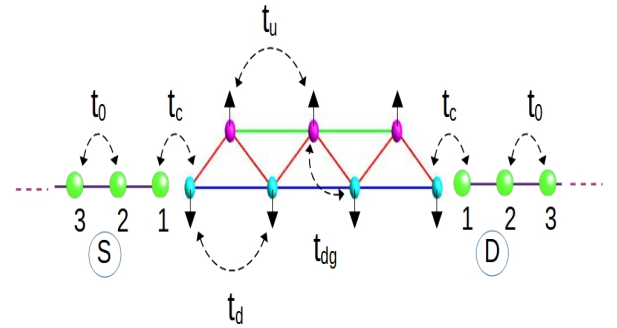


FIG. 1: (Color online). The schematic illustration presents a triangular spin ladder connected to source and drain electrodes. This unique configuration opens a new frontier in thermoelectric transport by capturing interplay between diagonal hopping and onsite energy.

setup, and their sum yields a transparent decomposition of the total Hamiltonian. For completeness, the physical significance of each contribution is summarized below.

The sub-Hamiltonians H_S and H_D appearing in Eq. (1), which describe the source and drain electrodes, respectively, are given by

$$H_S = \sum_{n \leq -1} a_n^\dagger \epsilon_0 a_n + \sum_{n \leq -1} (a_n^\dagger t_0 a_{n-1} + a_{n-1}^\dagger t_0 a_n) \quad (2)$$

and

$$H_D = \sum_{n \geq 1} b_n^\dagger \epsilon_0 b_n + \sum_{n \geq 1} (b_n^\dagger t_0 b_{n+1} + b_{n+1}^\dagger t_0 b_n) \quad (3)$$

Here, t_0 and ϵ_0 denote the matrices $\text{diag}\{t_0, t_0\}$ and $\text{diag}\{\epsilon_0, \epsilon_0\}$, respectively. The parameter t_0 represents the nearest-neighbor hopping amplitude, whereas ϵ_0 is the on-site energy of the nonmagnetic electrodes.

The tunneling contribution H_{tn} is constructed in an analogous manner. As shown schematically in Fig. 1, the source electrode is coupled to the first site of the SSH chain, while the drain electrode is connected to the terminal site m . Under these considerations, the tunneling Hamiltonian H_{tn} takes the form

$$H_{tn} = (a_{-1}^\dagger t_s c_1 + c_m^\dagger t_d b_1 + \text{h.c.}) \quad (4)$$

where $t_s = \text{diag}\{t_s, t_s\}$ and $t_d = \text{diag}\{t_d, t_d\}$. The parameters t_s and t_d characterize the tunneling amplitudes between the central conductor (chain) and the source (S) and drain (D) electrodes, respectively.

The triangular ladder system is described within a tight-binding framework, where the spin degree of freedom is effectively mapped onto the spatial structure of the ladder. The upper leg accommodates only spin-up electrons, while the lower leg supports exclusively spin-down electrons. The total Hamiltonian of the ladder can be written as

$$H_L = H_{U,\uparrow} + H_{D,\downarrow} + H_\Delta, \quad (5)$$

where H_{\uparrow} and H_{\downarrow} correspond to the upper and lower legs, respectively, and H_{Δ} accounts for the diagonal (triangular) couplings between the two legs.

The Hamiltonian for the upper leg (spin-up channel) is given by

$$H_{U,\uparrow} = \sum_n (\epsilon_{\uparrow} - h \cdot \sigma) c_{n,\uparrow}^\dagger c_{n,\uparrow} - \sum_n t_u (c_{n+1,\uparrow}^\dagger c_{n,\uparrow} + \text{H.c.}), \quad (6)$$

where $c_{n,\uparrow}^\dagger$ ($c_{n,\uparrow}$) creates (annihilates) a spin-up electron at site n of the upper leg, ϵ_n^\uparrow denotes the onsite energy, and t_n^\uparrow is the nearest-neighbor hopping amplitude along the upper arm.

Similarly, the lower leg (spin-down channel) is described by

$$H_{D,\downarrow} = \sum_n (\epsilon_{\downarrow} + h \cdot \sigma) c_{n,\downarrow}^\dagger c_{n,\downarrow} - \sum_n t_d (c_{n+1,\downarrow}^\dagger c_{n,\downarrow} + \text{H.c.}), \quad (7)$$

where ϵ_n^\downarrow and t_n^\downarrow are the corresponding onsite energies and hopping integrals for the lower leg. The term $h \cdot \sigma$ describes the spin-dependent scattering processes in the system, where σ represents the Pauli spin vector and σ_z is taken to be diagonal. Under the assumption that all localized magnetic moments are uniformly aligned along the $\pm Z$ direction, the spin interaction term simplifies considerably.

The triangular geometry is introduced through diagonal inter-leg couplings, which connect site n of one leg to site $n+1$ of the opposite leg, and is described by

$$H_{\Delta} = - \sum_n t_{dg} (c_{n+1,\uparrow}^\dagger c_{n,\downarrow} + c_{n+1,\downarrow}^\dagger c_{n,\uparrow} + \text{H.c.}), \quad (8)$$

where t_{dg} denotes the diagonal hopping amplitude that generates the triangular ladder connectivity.

This construction ensures a strict spatial separation of spin channels, while the diagonal couplings enable controlled spin-dependent interference pathways. Such a geometry provides a natural platform for engineering spin-selective quantum transport and enhanced thermoelectric response.

B. Theoretical Framework

In this subsection, we outline the theoretical formalism used to compute the thermoelectric response of the system. Our analysis is based on the spin-resolved transmission probabilities of the nanojunction. We begin by defining the transmission function and subsequently describe, in a systematic manner, how the relevant thermoelectric coefficients are obtained from it.

Spin-Resolved Transmission Characteristics: The spin-dependent transport properties of the nanojunction are analyzed within the Green's function framework, which provides a rigorous and unified description of quantum transport while explicitly incorporating the influence of the electrodes. In this formalism, the retarded (advanced) Green's function of the central region is given

by

$$G^r = (G^a)^\dagger = [EI - H_R - \Sigma_S - \Sigma_D]^{-1}, \quad (9)$$

where Σ_S and Σ_D denote the self-energy matrices arising from the source and drain electrodes, respectively. These terms effectively encode the open-boundary conditions imposed by the contacts and account for the finite lifetime of electronic states due to their coupling with the leads. Here, I is the identity matrix and E represents the energy of the incident electron.

Once the Green's functions are known, the spin-resolved transmission probabilities can be computed directly as

$$\tau^{\sigma\sigma'} = \text{Tr} \left[\Gamma_S^\sigma G^r \Gamma_D^{\sigma'} G^a \right], \quad (10)$$

where $\tau^{\sigma\sigma'}$ denotes the probability for an electron entering the system with spin σ to exit with spin σ' . The case $\sigma = \sigma'$ corresponds to spin-conserving transport, whereas $\sigma \neq \sigma'$ captures spin-flip scattering processes. The spin-dependent coupling matrices Γ_S^σ and $\Gamma_D^{\sigma'}$ quantify the hybridization strength between the central region and the respective electrodes and are obtained from the self-energy matrices via

$$\Gamma_{S(D)}^{\sigma\sigma'} = i \left[\Sigma_{S(D)}^{\sigma\sigma'} - \left(\Sigma_{S(D)}^{\sigma\sigma'} \right)^\dagger \right]. \quad (11)$$

By incorporating both spin-preserving and spin-mixing channels, the effective transmission probabilities for the two spin sectors can be compactly expressed as

$$\tau^\uparrow = \tau^{\uparrow\uparrow} + \tau^{\uparrow\downarrow}, \quad \tau^\downarrow = \tau^{\downarrow\downarrow} + \tau^{\downarrow\uparrow}. \quad (12)$$

Thermoelectric Response Functions: To elucidate the thermoelectric performance of the system, we evaluate the spin-resolved Seebeck coefficient, electrical conductance, and electronic thermal conductance within the Landauer–Büttiker formalism. These key transport coefficients are expressed as

$$S^{\uparrow(\downarrow)} = - \frac{1}{eT} \frac{L_1^{\uparrow(\downarrow)}}{L_0^{\uparrow(\downarrow)}}, \quad (13)$$

$$G^{\uparrow(\downarrow)} = e^2 L_0^{\uparrow(\downarrow)}, \quad (14)$$

$$K_{el}^{\uparrow(\downarrow)} = \frac{1}{T} \left(L_2^{\uparrow(\downarrow)} - \frac{\left(L_1^{\uparrow(\downarrow)} \right)^2}{L_0^{\uparrow(\downarrow)}} \right). \quad (15)$$

The Landauer integrals L_n ($n = 0, 1, 2$), which form the backbone of the thermoelectric analysis, are defined as^{41,42}

$$L_n^{\uparrow(\downarrow)} = - \frac{1}{h} \int \tau^{\uparrow(\downarrow)} \left(\frac{\partial f(E)}{\partial E} \right) (E - E_F)^n dE, \quad (16)$$

where $f(E)$ is the Fermi–Dirac distribution function and E_F denotes the equilibrium Fermi energy. Using these

quantities, the charge and spin thermoelectric coefficients are constructed in a transparent manner. The charge and spin Seebeck coefficients are given by^{41,42}

$$S_C = \frac{S^\uparrow + S^\downarrow}{2}, \quad S_S = S^\uparrow - S^\downarrow, \quad (17)$$

while the corresponding electrical conductances read

$$G_C = G^\uparrow + G^\downarrow, \quad G_S = G^\uparrow - G^\downarrow. \quad (18)$$

The electronic thermal conductance takes the form

$$K_C = K_S = K^\uparrow + K^\downarrow = K. \quad (19)$$

Owing to the nanoscale size of the system under consideration, the phonon-mediated thermal conductance K_{ph} is expected to be negligibly small. We therefore neglect its contribution and, without loss of generality, identify the total thermal conductance with its electronic component, i.e., $K_e = K_C = K_S = K$.

Finally, the efficiency of thermoelectric energy conversion is quantified through the charge and spin figures of merit, defined as

$$Z_C T = \frac{S_C^2 G_C T}{K}, \quad Z_S T = \frac{S_S^2 G_S T}{K}. \quad (20)$$

III. NUMERICAL RESULTS AND DISCUSSION

In this section, we present a comprehensive numerical study of the thermoelectric transport properties of the proposed model as shown in Fig. 1, identifying parameter regimes that yield substantially enhanced thermoelectric performance, as reflected by large values of the figure of merit ZT . Our analysis demonstrates that the combined effects of hopping modulation and periodic or aperiodic onsite potentials play a central role in shaping the electronic transport characteristics and thermoelectric efficiency. By systematically tuning these parameters, we show how both charge and spin thermoelectric responses can be effectively optimized, providing concrete design guidelines for high-performance low-dimensional thermoelectric systems. Unless stated otherwise, the system size is fixed at $N = 21$, the onsite energy of the leads is set to $\epsilon_0 = 0$, and the lead hopping strength is chosen as $t_0 = 2$. The coupling between the conductor and the source and drain electrodes is taken as $t_S = t_D = 0.8$, ensuring symmetric and stable contact conditions. All calculations are performed at room temperature ($T = 300$ K), and energies are expressed in units of electron-volts (eV). Parameter values specific to individual analyses are indicated where appropriate.

Impact of upper-arm hopping t_u

A. Spectral Profile of the Transmission Function

We begin our analysis by examining the energy-dependent transmission function $\mathcal{T}(E)$ under controlled

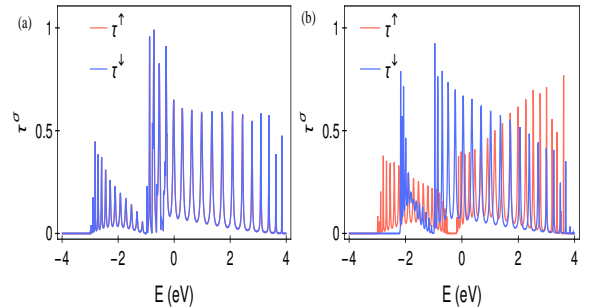


FIG. 2: (Color online). The plot illustrates the transmission function as a function of energy under various hopping configurations. Panel (a) displays fully spin-overlapped transmission spectra, indicating the absence of spin-dependent separation when the hopping amplitude is $t_u = 1$. In contrast, panel (b) shows partial overlap between the spin-resolved channels, with $t_u = 0.6$, clearly revealing the onset of spin-channel differentiation. This behavior reflects the subtle interplay between the distinct hopping pathways and their collective influence on spin-dependent transport characteristics.

variations of the hopping parameter t_u . When all hopping amplitudes are identical, i.e., $t_d = t_{dg} = t_u = 1$ eV the transmission spectra for the up- and down-spin channels are completely overlapped, as shown in Fig. 2(a), indicating the absence of spin-dependent transport. In contrast, when $t_d = t_{dg} = 1$ eV and $t_u = 0.6$ eV a distinct partial separation between the up- and down-spin transmission spectra emerges [see Fig. 2(b)]. This behavior clearly demonstrates that tuning t_u serves as an effective means to control spin-selective transmission.

The origin of this spin-dependent asymmetry lies in the breakdown of geometric and hopping symmetry. When all hopping amplitudes are uniform, the structure remains symmetric for both spin orientations, resulting in identical transport characteristics. However, reducing t_u disrupts this balance, leading to different effective environments for up- and down-spin electrons. The effect is more pronounced for the down-spin channel, which is more strongly influenced by t_u . Consequently, the resulting asymmetry in hopping strengths induces distinct spin-resolved transmission paths. Such control over spin-channel separation is particularly advantageous for optimizing spin thermoelectric efficiency, as minimal overlap between up- and down-spin transmissions is a prerequisite for achieving a large spin-dependent figure of merit. These results therefore highlight the strong potential of the present model for realizing efficient spin thermoelectric generators.

B. Fermi-energy dependence of the Seebeck coefficient

We next calculate the Seebeck coefficients for both spin channels. For this analysis, we adopt the same hopping parameters as in Fig. 2(d), which are retained throughout the remainder of the study unless otherwise specified. The corresponding charge and spin Seebeck coefficients are then evaluated using Eq. 17. To elucidate the origin

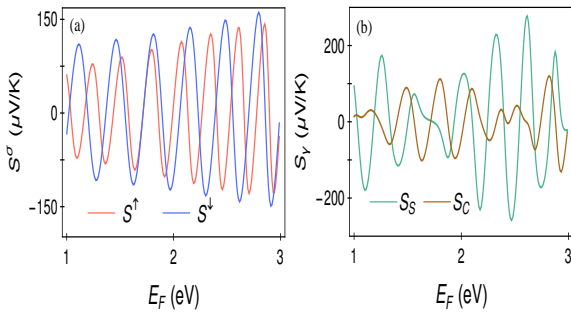


FIG. 3: (Color online). Seebeck coefficient as a function of Fermi energy is shown. Panel (a) displays the spin-resolved Seebeck response, showing distinct contributions from the up- and down-spin channels. Panel (b) presents the corresponding charge and spin Seebeck coefficients, thereby capturing the combined thermoelectric behavior arising from both transport channels.

and behavior of the Seebeck responses and their spin-resolved components, we analyze the central part of the Landauer integral, expressed as $\tau^\sigma(E) \left(\frac{\partial f}{\partial E} \right) (E - E_F)$, for each spin channel. The presence of the $(E - E_F)$ term naturally allows S^σ to assume both positive and negative values depending on the position of the Fermi energy E_F . As shown in Fig. 3(a), the spin-resolved Seebeck coefficients exhibit a pronounced asymmetry in both magnitude and sign, with the up- and down-spin components contributing oppositely across a wide energy range. These distinct spin contributions combine to yield the total charge and spin Seebeck coefficients, S_γ (with $\gamma = C, S$), displayed in Fig. 3(b). Owing to the negative sign in Eq. 13, the Seebeck coefficient varies inversely with the spin-resolved transmission function τ^σ , hence, rising edges in τ^σ , correspond to trailing features in S^σ , and vice versa. This interplay results in well-separated peaks in the Seebeck spectra, arising from the offset between the rising and falling edges of τ^\uparrow and τ^\downarrow . When t_u differs from the other hopping parameters, the symmetry between the up- and down-spin transmission channels is broken, leading to distinct line shapes and energy separations in their transmission spectra. As shown in Fig. 2(b), within the energy window 0 to 4 the crossing points of τ^\uparrow intersects τ^\downarrow coincide with opposite signs in S^\uparrow and S^\downarrow [see Fig. 3(a)]. Owing to their nearly opposite characteristics over a wide energy range, a sizable spin Seebeck coefficient S_S naturally emerges, surpassing the charge counterpart S_C , as evident in Fig. 3(b). Quantitatively, the charge Seebeck coefficient reaches a maximum of approximately $120 \mu\text{V}/\text{K}$, whereas the spin Seebeck coefficient attains nearly $270 \mu\text{V}/\text{K}$. A comprehensive analysis across the full Fermi energy range confirms that S_S consistently dominates over S_C . Since the Seebeck coefficient enters quadratically in the numerator of the thermoelectric figure of merit $Z_\gamma T$ [Eq. 20], its magnitude plays a decisive role in determining the overall thermoelectric efficiency. The observed large S_S and comparatively smaller S_C thus directly lead to a substantial enhancement of $Z_S T$ relative to $Z_C T$, as discussed in the subsequent subsection. These results clearly

demonstrate that a controlled asymmetry between the spin-resolved transmission functions, together with their minimal overlap, can be strategically exploited to achieve a strong and tunable spin Seebeck response.

C. Fermi-energy dependence of electrical and thermal conductances

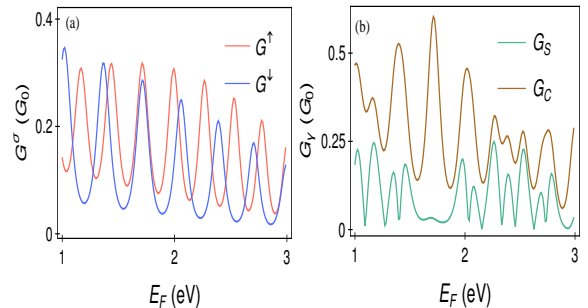


FIG. 4: (Color online). Panel (a) presents the spin-resolved electronic conductance as a function of Fermi energy, clearly illustrating the distinct contributions from the up- and down-spin carriers. Panel (b) compares the corresponding total charge and spin conductances, offering insight into the system's thermoelectric response arising from spin-dependent transport channels.

In this subsection, we investigate two additional thermoelectric quantities, electrical and thermal conductances which play a fundamental role in determining the efficiency of energy conversion in nanoscale systems. To ensure consistency and facilitate meaningful comparison, our analysis focuses on the same energy window as before, spanning 1-3 eV where the overlap between the up- and down-spin transmission channels remains narrow. As expected from their physical definition, conductances are positive-definite, and our calculations confirm this behavior for both spin-resolved components. As shown in Fig. 4(a), the spin-dependent electrical conductances G^\uparrow and G^\downarrow remain positive throughout the entire energy range, demonstrating robust and spin-selective transport. The asymmetry between these channels originates from choosing t_u different from the other hopping parameters, which breaks the spin symmetry in the transmission spectra. The conductance profiles closely follow the features of the corresponding transmission functions, leading to multiple energy regions where G^\uparrow and G^\downarrow exhibit partial overlap. Since conductance is inherently positive, Eq. 18 provides a straightforward means of comparing the total charge and spin contributions. As depicted in Fig. 4(b), the charge conductance G_C consistently exceeds its spin counterpart G_S , with typical values of $G_C \approx 0.6 G_0$ and $G_S \approx 0.25 G_0$. This relatively higher G_C contributes favorably to the charge figure of merit $Z_C T$. However, because the spin Seebeck coefficient S_S is substantially larger than the charge Seebeck coefficient S_C , the overall thermoelectric efficiency in the spin channel remains superior. The enhanced S_S thus plays a decisive role in elevating the spin-dependent figure of merit $Z_S T$ beyond its charge-based analogue, underscoring the potential of

spin-polarized transport for high-efficiency thermoelectric applications.

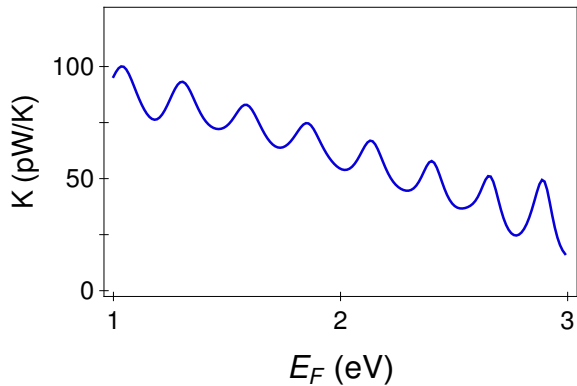


FIG. 5: (Color online). Thermal conductance as a function of Fermi energy, providing a comprehensive view of the system's thermoelectric transport characteristics.

The behavior of the thermal conductance is shown in Fig. 5. Both charge and spin channels yield identical values of K , indicating that thermal conductance does not independently influence Z_{CT} and Z_{ST} . Nevertheless, minimizing K remains crucial for improving the overall thermoelectric efficiency, as it appears in the denominator of Eq. 20. In our numerical analysis, the peak thermal conductance reaches approximately 100 pW/K. The variation of K with Fermi energy closely follows the general trend of the charge conductance G_C , though the proportionality between the two is not exact across the full energy range. This departure from proportionality signals a clear violation of the Wiedemann–Franz (WF) law^{43,44}, a feature frequently associated with enhanced thermoelectric performance in low-dimensional and nanoscale systems, and consistent with recent theoretical and experimental observations. It is important to emphasize that the present analysis considers only the electronic contribution to the thermal conductance. The phononic component has been deliberately omitted, as its effect is expected to be negligible due to the small system size under investigation.

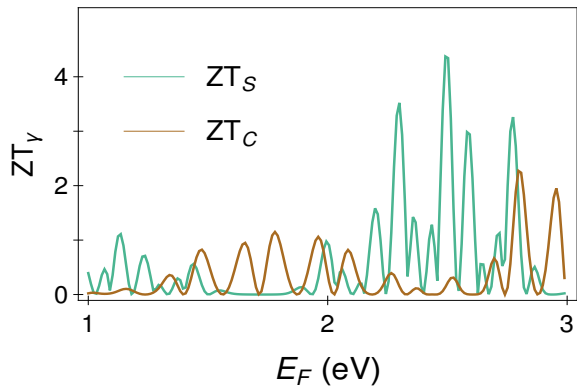


FIG. 6: (Color online). Thermoelectric figure of merit (ZT) as a function of Fermi energy. Both spin and charge ZT are shown.

D. Tunable charge and spin figure of merits (Z_{CT} , Z_{ST}) with Fermi energy

Building upon the detailed analysis of the thermoelectric quantities presented above, we now examine the variation of the charge and spin figures of merit, as shown in Fig. 6. The green and brown curves correspond to the spin and charge responses, respectively. A pronounced and systematic enhancement of Z_{ST} over Z_{CT} is evident throughout the Fermi energy window ranging from 1 to 3 eV. Quantitatively, while the charge figure of merit Z_{CT} reaches a maximum of approximately 2, its spin counterpart, Z_{ST} , attains a substantially higher peak value of nearly 4. This significant improvement in Z_{ST} originates from the considerably larger spin Seebeck coefficient (S_S) compared to the charge Seebeck coefficient (S_C), a feature that directly stems from the intrinsic asymmetry between the spin-resolved transmission functions. As discussed earlier, the energy regions close to the crossing points of the up- and down-spin transmission spectra play a pivotal role in enhancing the spin thermoelectric response, as they naturally promote opposite spin contributions to the thermopower. The combined effect of transmission asymmetry and spin-channel separation thus provides a robust pathway toward optimizing spin-dependent thermoelectric efficiency. In the subsequent section, we further analyze how controlled variations in the hopping parameters govern this asymmetry, offering a deeper microscopic understanding of the tunability and design principles underlying efficient spin-selective thermoelectric devices based on such ladder-like geometries.

Impact of diagonal hopping

In this subsection, we analyze the influence of the diagonal hopping amplitude under the condition $t_u \neq t_d$ on the thermoelectric performance of the system. Introducing a finite diagonal hopping term modifies the available conduction pathways and consequently the quantum interference patterns. Since the upper and lower arms of the ladder structure host opposite spin species, up spin in the upper arm and down spin in the lower, independent tuning of t_u , t_d and t_{dg} explicitly breaks the spin-channel symmetry. This asymmetry reshapes the transmission spectrum and can substantially enhance the spin-dependent thermoelectric coefficients. Physically, the simultaneous variation of arm and diagonal hoppings opens multiple interfering trajectories for spin transport. The resulting transmission asymmetry not only increases the magnitude of thermoelectric response but also shifts the Fermi-energy window where maximal values of ZT are achieved. Thus, controlled manipulation of hopping parameters provides a powerful handle to optimize spin-selective thermoelectric efficiency in ladder-type quantum systems.

We begin our analysis by examining the energy-dependent transmission function $\mathcal{T}(E)$ systematic variations of the diagonal hopping amplitude t_{dg} . In Fig. 7, we present the transmission spectra for $t_d = 1$, $t_u = 0.6$ and $t_{dg} = 0.5$ eV. A clear departure from the behavior shown

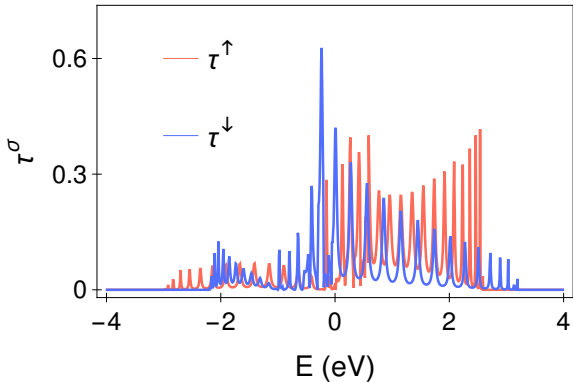


FIG. 7: (Color online). The plot illustrates the transmission function as a function of energy under variation of diagonal hopping. It shows partial overlap between the spin-resolved channels, with $t_u = 0.6$, $t_d = 1$ and $t_{dg} = 0.5$. This behavior reflects the subtle interplay between the distinct hopping pathways and their collective influence on spin-dependent transport characteristics.

in Fig. 2 is observed. In particular, the overlap between the spin-resolved transmission channels increases relative to the uniform-hopping case, highlighting the sensitivity of spin transport to the diagonal hopping strength. This trend indicates that t_{dg} serves as an effective tuning parameter for manipulating spin-dependent transport pathways.

The origin of the resulting asymmetry can be traced to the breakdown of geometric and hopping symmetry. In the fully symmetric configuration (Fig. 2), equal hopping amplitudes ensure identical electronic environments for up- and down-spin carriers, leading to spin-degenerate transmission. In contrast, reducing t_u breaks this balance by modifying the effective propagation channel for up-spin electrons. Introducing or varying t_{dg} further perturbs the interference conditions, producing a stronger distortion of the transmission line shape and enhancing the mixing between the spin-up and spin-down spectra.

Such controlled manipulation of spin-channel separation is particularly advantageous for spin thermoelectric applications. Since a minimal overlap between the two spin channels is a key requirement for achieving a large spin-dependent figure of merit, the present results demonstrate that adjusting t_{dg} provides a practical route toward optimizing spin-selective thermoelectric performance. Overall, these findings underscore the potential of the proposed ladder geometry as a platform for realizing efficient spin thermoelectric generators.

E. Evolution of the Seebeck coefficient across the Fermi energy

We next calculate the Seebeck coefficients for both spin channels Fig. 8. For this analysis, we adopt the same hopping parameters as in Fig. 7, which are retained throughout the remainder of the study unless otherwise specified. The corresponding charge and spin Seebeck coefficients are then evaluated using Eq. 17. We calculate the See-

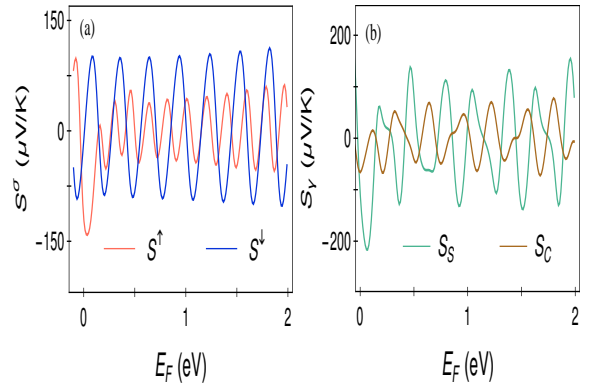


FIG. 8: (Color online). Seebeck coefficient as a function of Fermi energy is shown. Panel (a) displays the spin-resolved Seebeck response, showing distinct contributions from the up- and down-spin channels. Panel (b) presents the corresponding charge and spin Seebeck coefficients, thereby capturing the combined thermoelectric behavior arising from both transport channels.

beck coefficient following similar procedure as mentioned in the previous subsections. Quantitatively, the charge Seebeck coefficient reaches a maximum of approximately $150 \mu\text{V/K}$, whereas the spin Seebeck coefficient attains nearly $220 \mu\text{V/K}$. A comprehensive analysis across the full Fermi energy range confirms that S_S consistently dominates over S_C . Since the Seebeck coefficient enters quadratically in the numerator of the thermoelectric figure of merit $Z\gamma T$ [Eq. 20], its magnitude plays a decisive role in determining the overall thermoelectric efficiency. The observed large S_S and comparatively smaller S_C thus directly lead to a substantial enhancement of Z_{ST} relative to Z_{CT} , as discussed in the subsequent subsection. These results clearly demonstrate that a controlled asymmetry between the spin-resolved transmission functions, together with their minimal overlap, can be strategically exploited to achieve a strong and tunable spin Seebeck response.

We next evaluate the Seebeck coefficients for both spin channels using the same hopping parameters employed in Fig. 7, which remain fixed throughout the remainder of this work unless stated otherwise. The charge and spin Seebeck coefficients are computed from Eq. 17, following the procedure outlined in the preceding subsections. Quantitatively, the charge Seebeck coefficient S_C exhibits a maximum value of approximately $150 \mu\text{V/K}$, whereas the spin Seebeck coefficient S_S reaches nearly $220 \mu\text{V/K}$. A detailed examination across the entire Fermi-energy window reveals that S_S consistently surpasses S_C , reflecting the underlying asymmetry between the spin-resolved transmission spectra. Since the Seebeck coefficient enters quadratically in the numerator of the thermoelectric figure of merit $Z\gamma T$ [Eq. 20], its magnitude plays a crucial role in determining the overall thermoelectric performance. The substantially larger S_S , together with the comparatively smaller S_C , therefore directly accounts for the pronounced enhancement of Z_{ST} relative to Z_{CT} , as discussed in the following subsection. These findings clearly demonstrate that controlled

asymmetry in the spin-resolved transmission functions—combined with their reduced spectral overlap can be effectively leveraged to generate a strong and tunable spin Seebeck response. This establishes the present model as a promising platform for optimizing spin-dependent thermoelectric functionality.

F. Electrical and thermal conductances as functions of the Fermi energy

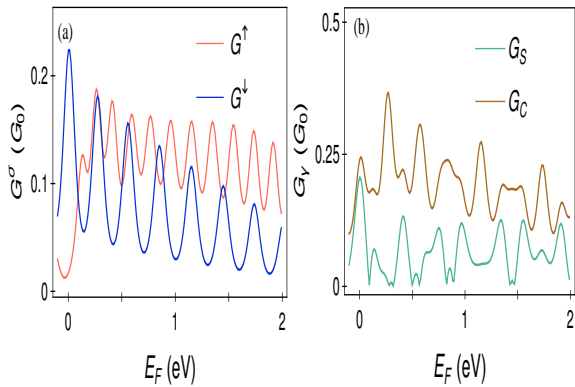


FIG. 9: (Color online). Panel (a) presents the spin-resolved electronic conductance as a function of Fermi energy, clearly illustrating the distinct contributions from the up- and down-spin carriers. Panel (b) compares the corresponding total charge and spin conductances, offering insight into the system’s thermoelectric response arising from spin-dependent transport channels.

In this subsection, we analyze two key thermoelectric quantities—the electrical and thermal conductances, Fig. 9 which are essential for evaluating the efficiency of energy conversion in nanoscale systems. As shown in Fig. 13(a), the spin-resolved electrical conductances, G^\uparrow and G^\downarrow , remain positive over the entire energy range, signifying stable and spin-selective transport. The asymmetry between these two channels arises from the choice of distinct onsite energies, $\epsilon_\uparrow \neq \epsilon_\downarrow$, which explicitly breaks spin symmetry in the transmission spectra. The conductance profiles closely mirror the corresponding transmission characteristics, giving rise to multiple energy regions where G^\uparrow and G^\downarrow partially overlap. Since conductance is intrinsically positive, Eq. (14) provides a straightforward means of comparing the total charge and spin contributions. As shown in Fig. 13(b), the charge conductance G_C consistently exceeds its spin counterpart G_S , with representative values of $G_C \approx 0.75 G_0$ and $G_C \approx 0.6 G_0$. The relatively larger G_C contributes positively to the charge figure of merit $Z_C T$. However, because the spin Seebeck coefficient S_S is considerably greater than the charge Seebeck coefficient S_C , the overall thermoelectric efficiency of the spin channel remains superior. The enhanced S_S thus plays a decisive role in elevating the spin-dependent figure of merit $Z_S T$ beyond its charge-based analogue, underscoring the promise of spin-polarized transport for high-efficiency thermoelectric applications.

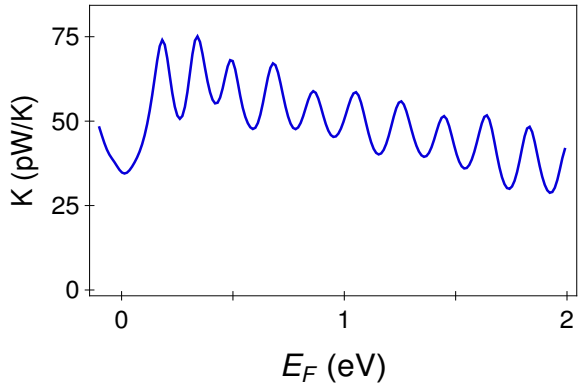


FIG. 10: (Color online). Thermal conductance as a function of Fermi energy, providing a comprehensive view of the system’s thermoelectric transport characteristics.

The behavior of the thermal conductance is presented in Fig. 10. Both charge and spin channels yield identical thermal conductance values, indicating that K does not directly differentiate $Z_C T$ and $Z_S T$. Nevertheless, minimizing K remains crucial for optimizing overall thermoelectric performance, as it appears in the denominator of Eq. (16). In our calculations, the peak thermal conductance reaches approximately 150 pW/K. It is important to note that the present analysis includes only the electronic contribution to K ; the phononic part has been neglected, as its effect is expected to be minimal owing to the small system size under consideration.

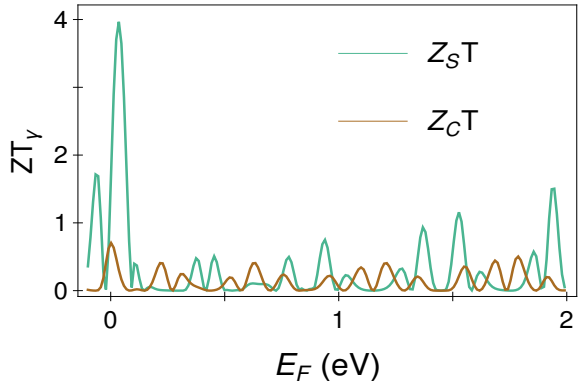


FIG. 11: (Color online). Thermoelectric figure of merit (ZT) as a function of Fermi energy. Both spin and charge ZT are shown and the parameters used are consistent with those in Fig. 2 (d).

Impact of binary type onsite energies

In this subsection, we examine an alternative route to induce spin asymmetry. Instead of introducing different hopping amplitudes along the upper and lower arms, we consider a binary configuration of on-site energies for the up- and down-spin channels. This arrangement inherently breaks the spin symmetry and gives rise to distinct transport characteristics for the two spin species.

G. Energy-resolved transmission spectrum

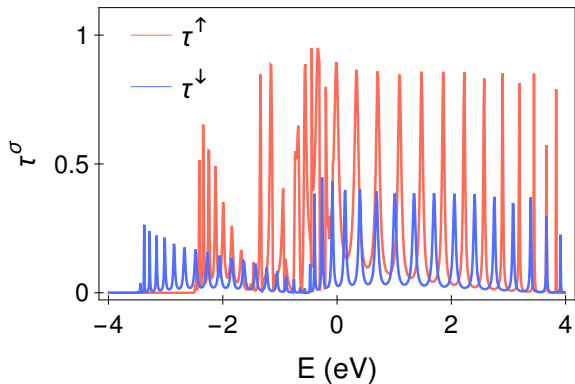


FIG. 12: (Color online). The plot illustrates the transmission function as a function of energy for different onsite energies. It reveals a partial overlap between the spin-resolved channels for $\epsilon_{\uparrow} = 0.5$ eV and $\epsilon_{\downarrow} = -0.5$ eV, clearly indicating the emergence of spin-channel differentiation. This behavior highlights the delicate interplay between the distinct onsite energy landscapes and their combined influence on spin-dependent transport characteristics.

We begin our analysis by examining the energy-dependent transmission function $\mathcal{T}(E)$, Fig. 12 focusing on the effect of spin-dependent onsite energies. When all hopping amplitudes are identical, i.e., $t_d = t_{dg} = t_u = 1$ eV, and the onsite energies are set to zero, the up- and down-spin transmission spectra completely overlap (not shown), indicating the absence of spin-dependent transport. In contrast, introducing distinct onsite energies, $\epsilon_{\uparrow} = 0.5$ eV and $\epsilon_{\downarrow} = -0.5$ eV, while keeping all hoppings equal, leads to a clear separation between the spin-resolved transmission spectra [see Fig. 6]. This behavior demonstrates that controlling the onsite energy asymmetry effectively modulates spin-selective transport.

The emergence of spin-dependent asymmetry originates from the breaking of the geometric and energetic equivalence between spin channels. In the uniform case, identical hoppings and onsite energies preserve full spin symmetry, resulting in degenerate transmission. However, the introduction of unequal onsite energies perturbs this balance, creating distinct local environments for up- and down-spin electrons and thus producing spin-resolved transmission pathways. Such control over spin-channel separation is crucial for enhancing spin thermoelectric performance, as reduced overlap between spin transmissions directly contributes to an increased spin-dependent figure of merit. These findings underscore the potential of this model in designing efficient spin-based thermoelectric generators.

H. Seebeck response as a function of Fermi energy

We next evaluate the Seebeck coefficients for both spin channels. In this analysis, we adopt the same set of hopping and onsite energy parameters as in Fig. 13, which are retained throughout this section unless otherwise stated.

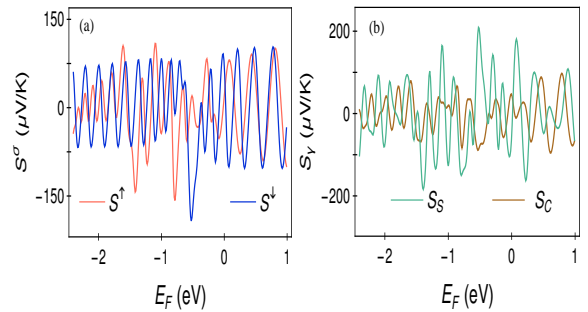


FIG. 13: (Color online). Seebeck coefficient as a function of Fermi energy is shown. Panel (a) displays the spin-resolved Seebeck response, showing distinct contributions from the up- and down-spin channels. Panel (b) presents the corresponding charge and spin Seebeck coefficients, thereby capturing the combined thermoelectric behavior arising from both transport channels.

The corresponding charge and spin Seebeck coefficients are computed using Eq. (13).

As discussed earlier, the presence of the $(E - E_F)$ term in Eq. (13) naturally allows the spin-resolved Seebeck coefficient S^{σ} to acquire both positive and negative values depending on the position of the Fermi energy E_F . As shown in Fig. 13(a), the spin-resolved Seebeck coefficients exhibit a distinct asymmetry in both magnitude and sign, with the up- and down-spin components contributing oppositely over a wide energy range. These contrasting spin contributions combine to yield the total charge and spin Seebeck coefficients, S_{γ} (with $\gamma = C, S$), displayed in Fig. 7(b).

Due to the negative sign in Eq. (9), the Seebeck coefficient varies inversely with the spin-resolved transmission function τ^{σ} rising edges in τ^{σ} correspond to trailing features in S^{σ} , and vice versa. This interplay leads to well-separated peaks in the Seebeck spectra, arising from the offset between the rising and falling edges of τ^{\uparrow} and τ^{\downarrow} . For instance, as seen in Fig. 6, around $E \approx -1.5$ eV, τ^{\uparrow} increases while τ^{\downarrow} decreases, resulting in the opposite trend in S^{\uparrow} and S^{\downarrow} in Fig. 13(a).

Owing to their largely opposing characteristics across a broad energy window, a sizable spin Seebeck coefficient S_S naturally emerges, surpassing its charge counterpart S_C , as evident from Fig. 13(b). Quantitatively, S_C attains a maximum of about $100 \mu\text{V}/\text{K}$, whereas S_S reaches nearly $200 \mu\text{V}/\text{K}$. A systematic inspection over the entire Fermi energy range confirms that S_S consistently dominates S_C .

Since the Seebeck coefficient enters quadratically in the numerator of the thermoelectric figure of merit $Z_{\gamma}T$ [Eq. (16)], its magnitude plays a decisive role in governing thermoelectric efficiency. The large S_S and comparatively smaller S_C thus directly contribute to the enhanced spin figure of merit Z_ST relative to its charge counterpart Z_{CT} , as discussed in the next subsection. These findings clearly establish that a controlled asymmetry between the spin-resolved transmission channels combined with their minimal overlap can be effectively exploited to achieve a robust and tunable spin Seebeck response.

I. Electrical and thermal conductances

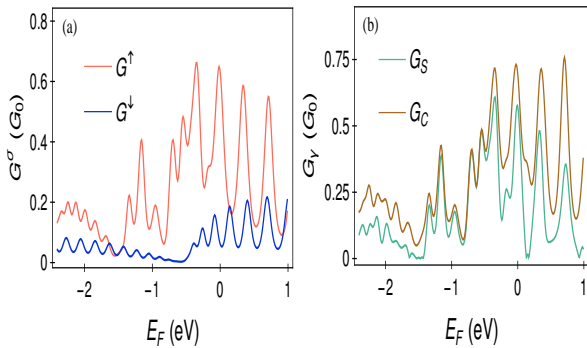


FIG. 14: (Color online). Panel (a) presents the spin-resolved electronic conductance as a function of Fermi energy, clearly illustrating the distinct contributions from the up- and down-spin carriers. Panel (b) compares the corresponding total charge and spin conductances, offering insight into the system’s thermoelectric response arising from spin-dependent transport channels.

In this subsection, we analyze two key thermoelectric quantities—the electrical Fig. 14 and thermal conductances which are essential for evaluating the efficiency of energy conversion in nanoscale systems. As shown in Fig. 8(a), the spin-resolved electrical conductances, G^\uparrow and G^\downarrow , remain positive over the entire energy range, signifying stable and spin-selective transport. The asymmetry between these two channels arises from the choice of distinct onsite energies, $\epsilon_\uparrow \neq \epsilon_\downarrow$, which explicitly breaks spin symmetry in the transmission spectra. The conductance profiles closely mirror the corresponding transmission characteristics, giving rise to multiple energy regions where G^\uparrow and G^\downarrow partially overlap. Since conductance is intrinsically positive, Eq. (14) provides a straightforward means of comparing the total charge and spin contributions. As shown in Fig. 8(b), the charge conductance G_C consistently exceeds its spin counterpart G_S , with representative values of $G_C \approx 0.75 G_0$ and $G_C \approx 0.6 G_0$. The relatively larger G_C contributes positively to the charge figure of merit $Z_C T$. However, because the spin Seebeck coefficient S_S is considerably greater than the charge Seebeck coefficient S_C , the overall thermoelectric efficiency of the spin channel remains superior. The enhanced S_S thus plays a decisive role in elevating the spin-dependent figure of merit $Z_S T$ beyond its charge-based analogue, underscoring the promise of spin-polarized transport for high-efficiency thermoelectric applications.

The behavior of the thermal conductance is presented in Fig. 15. Both charge and spin channels yield identical thermal conductance values, indicating that K does not directly differentiate $Z_C T$ and $Z_S T$. Nevertheless, minimizing K remains crucial for optimizing overall thermoelectric performance, as it appears in the denominator of Eq. (16). In our calculations, the peak thermal conductance reaches approximately 150 pW/K. It is important to note that the present analysis includes only the electronic contribution to K ; the phononic part has been neglected, as its effect is expected to be minimal owing

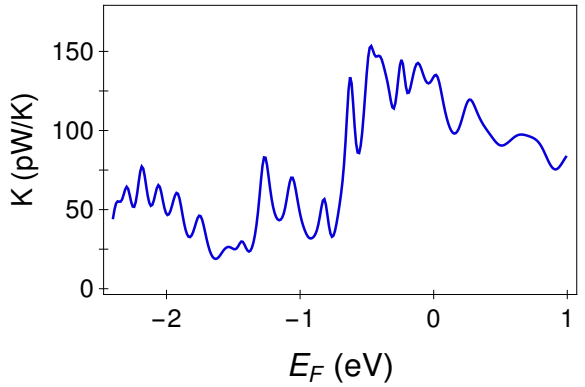


FIG. 15: (Color online). Thermal conductance as a function of Fermi energy, providing a comprehensive view of the system’s thermoelectric transport characteristics.

to the small system size under consideration.

J. Fermi Energy-resolved charge and spin figures of merit

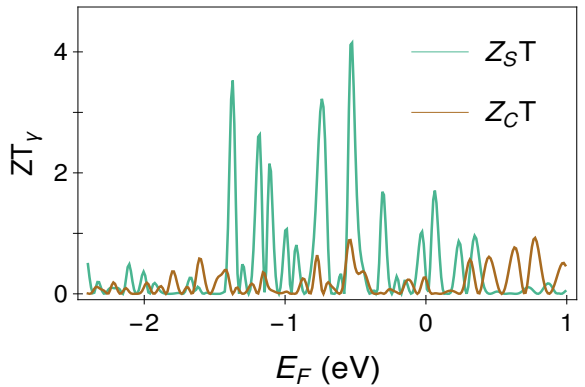


FIG. 16: (Color online). This figure presents the phase diagram of thermoelectric parameters as functions of both α and β . Panel (a) and (d) display the variation of the maximum values of the spin and charge thermoelectric figure of merit (ZT), respectively. Panels (b) and (e) illustrate the corresponding maximum values of the spin and charge Seebeck coefficients. Finally, panels (c) and (f) show the maximum spin and charge conductance. Together, these panels provide a comprehensive overview of how the thermoelectric response for both spin and charge channels is modulated by the interplay between α and β .

Building upon the preceding analysis of thermoelectric transport, we now examine the variation of the charge and spin figures of merit, as shown in Fig. 16. The brown and green curves represent the charge ($Z_C T$) and spin ($Z_S T$) responses, respectively Fig. 16. A systematic enhancement of $Z_S T$ over $Z_C T$ is observed throughout the Fermi energy range from -3 eV to 1 eV. Quantitatively, while $Z_C T$ reaches a maximum value of approximately 2, its spin counterpart attains nearly 4, demonstrating a substantial improvement in spin thermoelectric efficiency. This enhancement primarily arises from

the markedly larger spin Seebeck coefficient (S_S) compared to its charge counterpart (S_C), which originates from the intrinsic asymmetry between the spin-resolved transmission functions. As discussed earlier, the energy regions near the crossing points of the up- and down-spin transmission spectra play a crucial role, as they induce opposite spin contributions to the thermopower and thereby amplify S_S . The combined influence of transmission asymmetry and spin-channel separation thus provides an effective mechanism for achieving enhanced and tunable spin-dependent thermoelectric performance.

IV. CONCLUSION

In summary, we have developed a coherent theoretical framework to investigate spin-dependent thermoelectric transport in a triangular ladder geometry. By spatially segregating spin-up and spin-down channels and deliberately breaking the symmetry between the two arms, we achieve a controlled separation of spin-resolved transmission spectra. Within the NEGF formalism, we demon-

strate that minimizing spectral overlap and enhancing energy asymmetry between opposite-spin transmission functions leads to a pronounced enhancement of the spin-dependent Seebeck coefficient. Two complementary symmetry-breaking routes, spin-dependent onsite energy modulation and asymmetric hopping along the ladder arms, are shown to provide robust and flexible control over spin-resolved transport without invoking external magnetic fields. Our analysis reveals a strong sensitivity of spin thermoelectric efficiency to microscopic transport parameters, enabling systematic optimization of the spin figure of merit. The proposed model simultaneously supports efficient spin filtering and enhanced spin caloritronic response, offering a minimal yet highly tunable platform for engineering spin-selective transport in low-dimensional systems. The results highlight the crucial role of geometry, symmetry breaking, and quantum coherence in achieving high-performance spin thermoelectric functionality and open avenues for future studies incorporating correlation effects and topological design principles.

* Electronic address: ranjinibhattacharya@gmail.com

† Electronic address: souvikroy138@gmail.com

- ¹ G. S. Nolas, J. Sharp and J. Goldsmid, *Thermoelectrics: Basic Principles and New Materials Developments* (Springer, Berlin, 2001)
- ² A. F. Ioffe, *Semiconductor Thermoelements and Thermoelectric Cooling* (Infosearch Limited, London, 1957)
- ³ H. J. Goldsmid, *Introduction to Thermoelectricity* (Springer, New York, 2010)
- ⁴ F.J. DiSalvo, *Science* **285**, 703 (1999).
- ⁵ S. Riffat, X. Ma, *Appl. Therm. Eng.* **23**, 913 (2003).
- ⁶ JP. Thomas, MA. Qidwai and JC. Kellogg, *J. Power Sources* **159**, 1494 (2006).
- ⁷ A. Nadtochiy, V. Kuryliuk, V. Strelchuk, O. Korotchenkov, P. Li, and S. Lee, *Sci. Rep.* **9**, 16335 (2019).
- ⁸ C. Bhandari, D.M. Rowe, *CRC Handbook of Thermoelectrics*, (CRC Press, Boca Raton, FL, 1995, p. 49).
- ⁹ J. D. Song *et. al.*, *Scientific reports* **7**, 40026 (2017).
- ¹⁰ M. Xue *et. al.*, *Friction* **2**, 209 (2014).
- ¹¹ S. Das Sarma, and E. H. Hwang, *Physical Review B* **54**, 1936 (1996).
- ¹² H. B. Akkerman, P. W. Blom, D. M. De Leeuw, and B. De Boer, *Nature* **441**, 69 (2006).
- ¹³ R. Bhattacharya and S. K Maiti *J. Phys. D: Appl. Phys.* **56**, 075303 (2023).
- ¹⁴ M. Dresselhaus, G. Chen, M. Tang, R. Yang, H. Lee, D. Wang, Z. Ren, J.-P. Fleurial, and P. Gogna, *Adv. Mater.* **19**, 1043 (2007).
- ¹⁵ A. P. Ramirez, A. Hayashi, R.J. Cava, R. Siddharthan and B. S. Shastry, *Nature* **399**, 333 (1999).
- ¹⁶ H. A. Mook, P. Dai, S. M. Hayden, G. Aeppli, T. G. Perring and F. Dogan, *Nature* **395**, 580 (1998).
- ¹⁷ H. Adachi, K. I. Uchida, E. Saitoh, J. I. Ohe, S. Takahashi and S. Maekawa, *Appl. Phys. Lett.* **97**, 25 (2010).
- ¹⁸ Y. Wang, N.S. Rogado, R.J. Cava, and N.P. Ong, *Nature* **423**, 425 (2003).
- ¹⁹ N. Yoshida, *J. Phys. Commun.* **3**, 045013 (2019).
- ²⁰ C. Deranlot *et.al.*, *Science*, **327**, 1106 (2010).

²¹ G. A. Prinz, *Physics today* **48**, 58 (1995).

²² B. Z. Rameshti, and A. G. Moghaddam, *Physical Review B* **91**, 155407 (2015).

²³ L. Ding and Y. Zhong, *Phys. Chem. Chem. Phys.* **20**, 20228 (2018).

²⁴ K. Uchida, S. Takahashi, K. Harii, J. Ieda, W. Koshiba, K. Ando, S. Maekawa and E. Saitoh, *Nature* **455**, 778 (2008).

²⁵ M. Matsuo, Y. Ohnuma, T. Kato and S. Maekawa, *Phys. Rev. Lett.* **120**, 037201 (2018).

²⁶ D. D. Wu, H. H. Fu, Q. B. Liu and R. J. Wu, *Mater. Chem. C* **6**, 10603 (2018).

²⁷ P. Trocha and E. Siuda, *Sci. Rep.* **12**, 5348 (2022).

²⁸ K. Uchida *et. al.*, *Nat. Mater.* **9**, 894 (2010).

²⁹ H. Adachi, K. Uchida, E. Saitoh and S. Maekawa, *Rep. Prog. Phys.* **76**, 036501 (2013).

³⁰ Z. Gholami and F. Khoeini, *Sci. Rep.* **11**, 104 (2021).

³¹ A. Bhattacharya, *et. al.*, *Phys. Rev. Lett.* **116**, 097204 (2016).

³² J. Shi *et. al.*, *Phys. Rev. Lett.* **122**, 217204 (2009).

³³ R. Bhattacharya and S. Roy *J. Appl. Phys.* **138**, 184301 (2025).

³⁴ R. Bhattacharya and S. Roy *J. Appl. Phys.* **137**, 154301 (2025).

³⁵ H. Adachi, K. I. Uchida, E. Saitoh, J. I. Ohe, S. Takahashi and S. Maekawa, *Rep. Prog. Phys.* **76**, 036501 (2013).

³⁶ S. M. Wu, W. Zhang, A. Kc, P. Borisov, J. E. Pearson, J. S. Jiang, D. Lederman, A. Hoffmann and A. Bhattacharya, *Phys. Rev. Lett.* **116**, 097204 (2016).

³⁷ A. Kehlberger, U. Ritzmann, D. Hinzke, E. J. Guo, J. Cramer, G. Jakob, M. C. Onbasli, D. H. Kim, C. A. Ross, M. B. Jungfleisch, and B. Hillebrands, *Phys. Rev. Lett.* **115**, 096602 (2015).

³⁸ S. M. Wu, J. E. Pearson, and A. Bhattacharya, *Phys. Rev. Lett.* **114**, 186602 (2015).

³⁹ S. Datta. *Superlattices and microstructures* **28**, 253 (2000).

⁴⁰ J. S. Wang, B. K. Agarwalla, H. Li, and J. Thingna, *Frontiers of Physics*, **9**, 673 (2014).

⁴¹ M. Shirdel-Havar and R. Farghadan, Phys. Rev. B **97**, 235421 (2018).

⁴² F. Ildarabadi and R. Farghadan, Phys. Rev. B **103**, 115424 (2021).

⁴³ M. Zarenia, T.B. Smith, A. Principi, G. Vignale, Phys. Rev. B **99**, (2019).

⁴⁴ G.D. Mahan, M. Bartkowiak, Appl. Phys. Lett. **74**, 953 (1999).